LANGMUIR

Article

pubs.acs.org/Langmuir

Acetate-Induced Disassembly of Spherical Iron Oxide Nanoparticle Clusters into Monodispersed Core−Shell Structures upon Nanoemulsion Fusion

Ahmet Kertmen,[*,†,‡,⊥] Pau Torruella,[§] Emerson Coy,[‡] Luis Yate,[∥] Grzegorz Nowaczyk,[‡] Jacek Gapiński,[‡] Carmen Vogt,[⊥] Muhammet Toprak,[*,⊥] Sonia Estradé,[§] Francesca Peiró,[§] Sławomir Milewski,[†] Stefan Jurga,[‡] and Ryszard Andruszkiewicz[†]

[†]Department of Pharmaceutical Technology and Biochemistry, Gdansk University of Technology, G. Narutowicza 11/12, 80-233 Gdansk, Poland

[‡]NanoBioMedical Centre, Adam Mickiewicz University, Umultowska 85, 61-614 Poznan, Poland

[§]LENS-MIND-IN2UB, Departament d'Electronica, Universitat de Barcelona, Martí i Franquès 1, 08028 Barcelona, Spain

[∥]CIC biomaGUNE, Paseo Miramón 182, 20009 Donostia—San Sebastian, Spain

[⊥]Department of Applied Physics, KTH-Royal Institute of Technology, Roslagstullsbacken 21, SE-106 91 Stockholm, Sweden

Supporting Information

ABSTRACT: It has been long known that the physical encapsulation of oleic acid-capped iron oxide nanoparticles (OA−IONPs) with the cetyltrimethylammonium (CTA^+) surfactant induces the formation of spherical iron oxide nanoparticle clusters (IONPCs). However, the behavior and functional properties of IONPCs in chemical reactions have been largely neglected and are still not well-understood. Herein, we report an unconventional ligand-exchange function of IONPCs activated when dispersed in an ethyl acetate/acetate buffer system. The ligand exchange can successfully transform hydrophobic OA−IONP building blocks of IONPCs into highly hydrophilic, acetate-capped iron oxide nanoparticles (Ac−IONPs). More importantly, we demonstrate that the addition of silica precursors (tetraethyl orthosilicate and 3-aminopropyltriethoxysilane) to the acetate/oleate ligand-exchange reaction of the IONPs induces the disassembly of the IONPCs into monodispersed iron oxide−acetate−silica core−shell−shell (IONPs@acetate@SiO_2) nanoparticles. Our observations evidence that the formation of IONPs@acetate@SiO_2 nanoparticles is initiated by a unique micellar fusion mechanism between the Pickering-type emulsions of IONPCs and nanoemulsions of silica precursors formed under ethyl acetate buffered conditions. A dynamic rearrangement of the CTA^+−oleate bilayer on the IONPC surfaces is proposed to be responsible for the templating process of the silica shells around the individual IONPs. In comparison to previously reported methods in the literature, our work provides a much more detailed experimental evidence of the silica-coating mechanism in a nanoemulsion system. Overall, ethyl acetate is proven to be a very efficient agent for an effortless preparation of monodispersed IONPs@acetate@SiO_2 and hydrophilic Ac−IONPs from IONPCs.

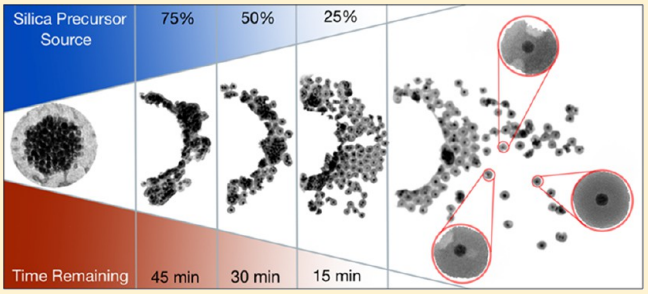

INTRODUCTION

In the last decade, surfactant-stabilized iron oxide nanoparticles (S-IONPs) synthesized by high-temperature (thermal decomposition) methods have gained increasing attention, thanks to their high degree of crystallinity, uniform size, well-defined surface composition, and long-term stability.[1−4] Such properties of the S-IONPs, which facilitate the development of standardized protocols, make them perfect candidates for biological applications requiring extensive safety evaluations. Moreover, additional advantages of thermal decomposition processes, such as large-scale production using nontoxic green precursors, make the S-IONPs the material of choice for IONP preparation.[1,5] However, hydrophobicity of the as-synthesized S-IONPs is the major drawback of using such particles in biological systems. To overcome the aqueous incompatibility of S-IONPs and enable their use in biological systems, hydrophilic and biocompatible surface-capping agents are required to cover the hydrophobic surface of nanoparticles.[1]

Ligand exchange is a widely used method to render S-IONPs aqueously compatible. This can be done by an exchange of initial hydrophobic stabilizers of IONPs with hydrophilic organic ligands[6−9] or by covering the nanoparticle surface with inorganic-capping agents.[10,11] Alternatively, encapsulation of the S-IONPs via physical (van der Waals or electrostatic)

Received: August 5, 2017
Revised: September 11, 2017
Published: September 12, 2017

DOI: 10.1021/acs.langmuir.7b02743
Langmuir 2017, 33, 10351−10365

interactions with amphiphilic lipids/surfactants or polymers[12,13] is commonly used. Even if differently classified from the application point of view, inorganic surface-capping and physical encapsulation processes are usually interconnected from the chemistry point of view. Physical encapsulation is usually used to render the hydrophobic nanoparticles aqueously dispersible, which is an important prerequisite for the inorganic surface-capping.[14] However, more importantly, physical encapsulation by amphiphilic agents can act as a template for the inorganic-capping layer formation of thick shells in a variety of shapes and morphologies.[14−18]

Coating the hydrophobic S-IONP surfaces with hydrophilic silica shells is a very specific example, where the inorganic surface-capping and physical encapsulation processes are used in conjunction. Silica coating is performed either in oil-in-water (microemulsion) systems[14,19] or in water-in-oil (reverse microemulsion) systems.[20,21] Although the oil-in-water systems require the physical encapsulation of the S-IONPs before the silica-coating reaction, the water-in-oil systems do not. Consequently, typical oil-in-water mechanisms are usually described as the direct coating of the silica shells on the physical encapsulation layer formed by amphiphilic ligands.[15] However, water-in-oil mechanisms are based on the complete ligand exchange between the silicon oxide species and the primary hydrophobic stabilizing ligands of the nanoparticles.[21−24] We have previously reported detailed oil-in-water[19] and water-in-oil methods[22] for silica coating of the oleate-stabilized iron oxide nanoparticles (OA−IONPs) in the monodispersed core−shell form (IONPs@SiO_2). Notably, water-in-oil methods are time-consuming (>24 h) and laborious; hence the shorter processing time of oil-in-water methods (∼4 h) makes it the method of choice for the preparation of IONPs@SiO_2. Nevertheless, none of the reports on current silica-coating studies presented up to date, neither for oil-in-water nor for water-in-oil systems, provided a strong experimental proof allowing for identification of the ligand-exchange type during the core−shell nanoparticle formation. Further experimental evidence to identify the mechanism underlying the nanoparticle surface coating with silica is still required to fully understand the dynamics of the ligand-exchange process.

On the other hand, oil-in-water methods are usually regarded as more problematic because they require physical encapsulation by the amphiphilic capping agents before the silica-coating process, and the surfactant-stabilized nanoparticles, such as OA−IONPs, are known to form iron oxide nanoparticle clusters (IONPCs) in the presence of amphiphilic encapsulation agents.[25−30] Partial and insufficient clustering problems make it impossible to obtain silica-coated iron oxide particles in a monodispersed core−shell form. Consequently, previously reported oil-in-water methods were restricted to specific cetyltrimethylammonium bromide (CTAB) surfactant-to-IONP concentration ([CTAB]/[IONP]) ratios to avoid clustering.[19] However, the exact determination of [CTAB]/[IONP] ratios is also laborious and costly. Nevertheless, the strict dependence of the OA−IONP concentrations on the particle size[21] makes the silica-coating processes reproducible with only 20% success rate under low OA−IONP and surfactant concentration conditions. Therefore, development of a more reliable, less costly, nonlaborious, and high-yielding method for IONPs@SiO_2 preparation is clearly required to make these valuable materials available for application-oriented studies.

By contrast, the use of low [CTAB]/[IONP] ratios was found to be crucial to obtain monodisperse IONPs@SiO_2[19,28] and high [CTAB]/[IONP] ratios were previously reported to yield IONPCs/silica core−shell structures (IONPCs@SiO_2).[28] Because both methods were based on the base-catalyzed silica condensation in an oil-in-water system, it was sensible to assume that [CTAB]/[IONP] ratios play a key role in monodisperse IONPs@SiO_2 preparation. However, most recently, it was shown that monodispersed IONPs@SiO_2 could be prepared under high [CTAB]/[IONP] ratio conditions with much higher success rates and yields.[31] Strikingly enough, using high [CTAB]/[IONP] ratios in an uncatalyzed oil-in-water system were seen to induce "apple bite-like" cavity formations on silica shells, unlike in low [CTAB]/[IONP] conditions. However, no attention was paid to the silica formation mechanism in the core−shell form in such a high [CTAB]/[IONP] ratio system.

Correspondingly, in this paper, we compare low[19] and high[31] concentration oil-in-water methods. We aim to investigate how the monodisperse IONPs@SiO_2 were successfully formed despite the existence of IONPCs, and whether the appearance of "apple bite-like" cavities on silica shells was related to the existence of IONPCs or not. Furthermore, investigation of other factors, such as the role of acetate as the smallest carboxylate ligand in silica condensation, is carried out. Ethyl acetate saponification reactions are commonly used to stabilize pH in silica-condensation studies,[14,32] and carboxylate species are among the most common organic compounds used in ligand-exchange studies of IONPs.[33−38] Furthermore, acetate is known to be an ethyl acetate saponification byproduct. Yet, the role of acetate has never been taken into account in any of the previously reported silica-condensation studies.[14,19] We investigate the ethyl acetate saponification impact on IONPCs and discuss how it affects the silica precursor (tetraethyl orthosilicate and 3-aminopropyltriethoxysilane) hydrolysis while regulating the pH value. Finally, we aim to understand the mechanism behind the silica formation in the presence of IONPCs by performing detailed experimental studies using transmission electron microscopy (TEM), Raman, Fourier transform infrared (FTIR), dynamic light scattering (DLS), and X-ray photoelectron spectroscopy (XPS) techniques. In the light of the obtained results, we elucidate whether the silica formation on OA−IONP surfaces is associated with direct ligand exchange, physical encapsulation, or inorganic surface-capping in an ethyl acetate buffered oil-in-water system. Finally, we aim to achieve the strongest experimental support for the silica shell-formation mechanisms in a high concentration oil-in-water system and discuss our findings in the light of the previously proposed mechanisms, obtaining new insights.

EXPERIMENTAL SECTION

Chemicals and Materials. The following reagents, solvents, and materials were acquired from Sigma-Aldrich Co.: CTAB (≥98%), ethyl acetate (anhyd. 99.8%), chloroform, tetraethylorthosilicate (TEOS, 99%), 3-(aminopropyl)triethoxysilane (APTES, ≥98%), *n*-hexane (99%), diethyl ether (99.5%), iron(II) acetate (95%), and dialysis tubing (cellulose ester membrane with molecular weight cutoff = 14 000). Ethane (≥99.95%) was obtained from Linde. The following reagents and solvents were purchased from Avantor Performance Materials Poland S.A. (formerly POCH S.A.): 2-propanol (99.7%), sodium hydroxide (99.8%), nitric acid (65%), hydrochloric acid (35−38%), ethanol (96%), acetic acid (glacial), and 2-propanol (99.7%).

Characterization Methods. For time-resolved TEM studies of the silica-coating process, the samples collected at different time

DOI: 10.1021/acs.langmuir.7b02743
Langmuir 2017, 33, 10351−10365

intervals of the process were acidified with aqueous 5% HNO_3 solution to stop the silica condensation, and then they were centrifuged at 0−5 °C with 13.2 rpm force to remove the reaction medium. The resulting concentrated sample was redispersed in ethanol (5 s sonication), then directly applied on 300 mesh copper (carbon film only) TEM grids, and left to dry in vacuum. The images were acquired on a JEOL JEM-1400 transmission electron microscope.

Raman spectroscopy measurements were performed with 488, 514, and 633 nm laser excitation using a Renishaw Raman spectrometer attached to a Leica optical microscope with a 50× objective lens. The spectra were recorded over 200−3200 cm^{-1} range with 10 s exposure to 5% laser power (~0.85 mW for 633 nm He−Ne laser) in extended modes.

FTIR spectra were recorded with a Tensor 27 (Bruker Optics) spectrometer. Samples were prepared as KBr pellets by applying pressure under a hydraulic press. Before each spectral acquisition session, the background was recorded with pure KBr pellets, and the recorded background spectra were subtracted from each spectrum. Water and CO_2 peaks were automatically removed by the OPUS software used to operate the spectrometer. The spectra were recorded with 2 cm^{-1} resolution by 512 scans in the 4000−200 cm^{-1} range.

High-resolution TEM (HRTEM) images, scanning TEM high-angle annular dark field (STEM-HAADF) images, and electron energy loss spectroscopy spectrum images (EELS-SI) were acquired by means of a JEOL ARM200 transmission electron microscope equipped with a field emission gun and a Gatan GIF Quantum EELS spectrometer. Elemental maps and quantification of the EELS data were performed with Gatan DigitalMicrograph software. Obtained SI were quantified using the Egerton method[39] after denoising by the principal component analysis.

For cryo-TEM experiments, vitrified specimens were prepared in a semiautomated Cryoplunge 3 system from Gatan. A microliter drop of the sample was deposited onto lacey carbon grids (Ted Pella) previously treated with a plasma cleaner to ensure high hydrophilicity of the supporting film. Excess water was removed by gentle blotting with a filter paper and then rapidly plunged into liquid ethane cooled by liquid nitrogen. Such prepared grids were transferred to a Gatan 626 cryo-holder and maintained at −170 °C. Cryo-TEM experiments were carried out with a JEOL JEM-1400 transmission electron microscope equipped with a 3k × 4k Gatan camera.

DLS measurements were performed by means of a standard ALV DLS setup consisting of a laser (Coherent OBIS 660 nm, operating at 5 mW), an ALV goniometer, an ALV 7000 digital correlator, and a PerkinElmer avalanche photodiode SPCM-AQR 13. CONTIN algorithm[40] was applied to analyze the measured correlation functions and obtain the size distribution functions. The measurements were performed at room temperature.

XPS studies were performed on a XPS-SPECS-Sage HR 100 system, working with a non-monochromatic X-ray source (Al Kα line of 1486.6 eV energy and 350 W). Particles were drop-casted on gold-coated glass (150 nm) and allowed to degas in vacuum.

Preparation of Oleic Acid-Capped Iron Oxide Nanoparticles (OA−IONPs). OA−IONPs were synthesized by the thermal decomposition of the iron oleate complex, according to a previously described method.[5] The iron oleate complex was prepared by dissolving 1.08 g of $FeCl_3{\cdot}H_2O$ and 3.65 g of sodium oleate in ethanol/water/*n*-hexane (3:4:7, v/v/v) and refluxing the mixture at 70 °C for 4 h. When the emulsion cooled down to room temperature, the iron oleate complex was separated from the aqueous phase. To make the phase separation faster, diethyl ether was used. The extracted organic phase was washed several times with Milli-Q water (18 MΩ·cm) and finally evaporated in vacuum.

OA−IONPs were prepared by refluxing 3.6 g of the iron oleate complex and 0.57 g of oleic acid in 20 g of 1-octadecene for 30 min at 325 °C. After cooling the resulting nanoparticle suspension down to room temperature, the nanoparticles were separated from 1-octadecene by diluting the dispersion in 1 part of *n*-hexane, which was followed by precipitation with 5 parts of ethanol upon centrifugation. This procedure was repeated until a clean supernatant was obtained. The resulting OA−IONPs with an oily appearance were dispersed in *n*-hexane and stored at 4 °C for later use.

To convert the oily form of OA−IONPs into a dry (powdered) form, the particles were dispersed in a chloroform/hexane mixture at least five times. Each chloroform/hexane dispersion of OA−IONPs was precipitated from ethanol by centrifugation. In each subsequent washing process, the amount of hexane was reduced by 20%. After the last chloroform/hexane wash, the nanoparticle precipitate was rinsed with pure acetone. After evaporation of the solvents, the resulting powder of OA−IONPs was kept at 4 °C for further use. The nanoparticles obtained through the above-described procedure are hereinafter called "dried oleic acid-capped iron oxide nanoparticles" (dOA−IONPs).

Preparation of IONPCs. IONPCs were prepared by a phase transfer of OA−IONPs under **high [CTAB]/[IONP] ratio conditions**, according to a slightly modified version of the method reported by Qiu et al.[28] Briefly, 0.28−0.34 mg of 12.4 nm OA−IONPs in hexane (depending on the concentration, it equals 15−40 μL of hexane stock solution) was further dispersed in 2 mL of chloroform, and this dispersion was added to a 20 mL round flask containing 5.5 mL of 0.135 M CTAB aqueous solution. The resulting emulsion was mixed with a magnetic stirrer until a homogenous mixture was obtained. The organic phase was removed by heating the mixture to 60 °C under a N_2 flow. A complete removal of the organic solvents was performed under vacuum.

Ligand Exchange by Acetate Ions in the Presence of IONPCs. To investigate the role of acetate ions as carboxylate ligands, ethyl acetate saponification reaction was carried out in the presence of IONPCs. After preparation of IONPCs described above, the volume of aqueous IONPC dispersion was increased to 50 mL using Milli-Q water in a 100 mL, two-necked round flask. The pH value of this dispersion was adjusted to 11−12 with 300 μL of 2 M NaOH solution. The alkaline dispersion of the IONPCs was then heated to 60 °C in an oil bath. Addition of 3 mL of ethyl acetate was followed by a controlled temperature increase to 72−76 °C, and the dispersion was refluxed for 3.15 h while stirring with a magnetic stirrer at 750 rpm stirring rate. Then, the resulting nanoparticle suspension was slowly cooled down to room temperature under continuous magnetic stirring (while keeping the flask in the oil bath). When the suspension cooled down to room temperature, the resulting acetate-capped iron oxide nanoparticles (Ac−IONPs) were placed into a cellulose membrane tubing and dialyzed against Milli-Q water for at least 4−5 days to remove excess CTA^+ molecules and byproducts. The dialysis solvent (water) was refreshed every 18−24 h during the dialysis process.

Preparation of IONPs@SiO_2. To demonstrate the pH stabilization effect of ethyl acetate and high [CTAB]/[IONP] ratio conditions resulting in IONPC formation, silica shell formation reaction was performed by addition of ethyl acetate *before the silica precursors*. This reaction is hereinafter referred to as "PREP1" (practically, PREP1 process is an extended version of the above-described acetate/oleate ligand-exchange reaction by addition of silica precursors, TEOS and APTES). In detail, PREP1 was prepared by dilution of the aqueous IONPC dispersion (as described above) to 50 mL using Milli-Q water in a 100 mL three-necked round flask. The pH value of the IONPC dispersion was adjusted to 11−12 by adding 0.3 mL of 2 M NaOH solution. Then 3 mL of ethyl acetate, 0.3 mL of TEOS, and 50 μL of APTES were consecutively added, and the mixture was refluxed at 72−76 °C in an oil bath for 3.15 h. The reaction mixture was stirred with a magnetic stirrer at 750 rpm rate. After cooling down the resulting nanoparticle suspension for 1 h under continuous magnetic stirring (while keeping the flask in a warm oil bath), the pH value of the mixture was brought to 3−4 by addition of 1.5 mL of 5% aqueous HNO_3 solution. The nanoparticles were separated from the aqueous solution by centrifugation at 18 000−24 000 rpm at 0 °C and washed three times with ethanol and two times with 2:1 ethanol/water (v/v) mixture with repeated centrifugal separations at −5 °C. Finally, the resulting core−shell structures were dispersed in ethanol and stored at −20 °C for further use.

To understand the effect of low [CTAB]/[IONP] ratio conditions in silica shell formation, silica-condensation reaction was performed by

DOI: 10.1021/acs.langmuir.7b02743
Langmuir 2017, 33, 10351−10365

addition of ethyl acetate *after the silica precursors*. This method was based on conditions originally described by Kim et al.[14] and Ye et al.[19] to prepare individually CTAB-encapsulated OA–IONPs (CTA–OA–IONPs)[28] instead of IONPCs. This reaction is hereinafter referred to as "PREP2". For the phase transfer of OA–IONPs, 60% reduced amount of CTAB (~45 mM) and approximately 40% reduced amount of OA–IONPs were used in comparison to concentrations used in the PREP1 reaction. The values of other parameters were kept unchanged. After the dilution of CTA–OA–IONPs to 50 mL using Milli-Q water, pH of the dispersion was adjusted to 11–12 with the addition of 0.3 mL of 2 M NaOH solution. It was followed by addition of 0.3 mL of TEOS, 50 μL of APTES, and 3 mL of ethyl acetate consecutively. Then, the mixture was refluxed at 70–80 °C for 3.15 h while stirring with a magnetic stirrer. The resulting nanoparticle suspension remained under continuous magnetic stirring for 1 h while slowly cooling down. The nanoparticles were separated from the aqueous solution by centrifugation at 18 000–24 000 rpm at 0 °C and washed three times with ethanol and two times with 2:1 ethanol/water (v/v) mixture with repeated centrifugal separations at −5 °C. Finally, the resulting core–shell structures were dispersed in ethanol and stored at −20 °C for further use.

Dialysis of IONPs@SiO_2. To purify the silica-coated nanostructures from excess CTA^+ molecules, a dialysis procedure was performed according to a slightly modified version of a previously described method.[41] Namely, IONPs@SiO_2 were dispersed in 50 mL of ethanol, 2-propanol, and 2 M acetic acid mixture (1:1:2, v/v/v) and transferred into the dialysis membrane tubing. The nanoparticles were dialyzed against 1 L of the same solvent mixture for 24 h. The process was repeated three times. The amount of IONPs@SiO_2 used in the dialysis was usually half the amount obtained after the PREP1 synthesis.

RESULTS AND DISCUSSION

TEM and Cryo-TEM Characterizations of OA–IONPs and IONPCs. TEM observations of the hexane-dispersed OA–IONPs synthesized by the thermal decomposition method showed that the particles were in a nearly monodispersed form (Figure 1A,B). Nanoparticle size distribution was extracted

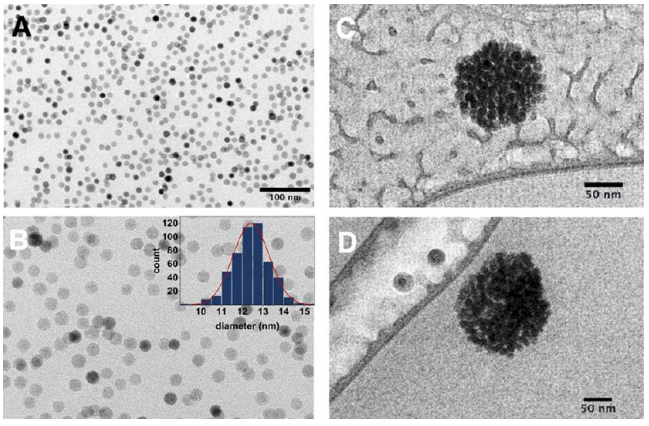

Figure 1. (A) Low-magnification TEM image of OA–IONPs, (B) high-magnification TEM image of OA–IONPs, where the inset shows their size distribution, and (C,D) cryo-TEM images of IONPCs (cryo-TEM grids were prepared using highly diluted dispersions of IONPCs).

from measurements of ≥500 individual particles using Fiji software.[42] The histogram demonstrated that the OA–IONPs had an average diameter of 12.4 ± 0.87 nm (Figure 1B inset).

Cryo-TEM observations confirmed that the physical encapsulation of OA–IONPs by CTAB molecules under high [CTAB]/[IONP] ratio conditions resulted in the formation of IONPCs having 100–200 nm diameter (Figure 1C,D).

FTIR and Raman Spectroscopy Analyses of Ac–IONPs and OA–IONPs. Impact of the in situ formed acetate species as potential carboxylate ligands on IONPCs was investigated by vibrational spectroscopies. FTIR analyses of the Ac–IONPs in comparison to OA–IONPs and dOA–IONPS revealed that the sample consisted of iron oxide and acetate/acetic acid species (detailed FTIR spectral analyses can be found in the Supporting Information Figure S1). Existence of the acetate/acetic acid species was evident from the highly hydrophilic nature of the IONPs after the reaction of IONPCs with ethyl acetate (Figure S2 in the Supporting Information).

Raman spectroscopy analysis was carried out separately for (inorganic) iron oxide and the organic content fingerprint regions in comparison to a series of reference organic compounds. These comparisons provided a much more clear evidence of the acetate/oleate ligand exchange. Raman spectral band assignments were made according to the literature data found for experimental and calculated/simulated spectroscopic properties of iron oxide structures (Figure 2).[43−48]

The 200–700 cm^{-1} fingerprint region of the iron oxide structures for Ac–IONPs and dOA–IONPs revealed at least five Raman active modes ($3T_{2g} + E_g + A_{1g}$) that belong to cubic inverse-spinel structure of magnetite (Figure 2A). The spectrum of dAO–IONPs shows identical band patterns as Ac–IONPs, however, the former resembles a convoluted form of the latter. Generally, Ac–IONP Raman spectrum showed similarities to the previously reported citrate-coated magnetite[49] spectrum, which strongly supports the existence of carboxylate species. The strongest peak of the Ac–IONP spectrum at 666 cm^{-1} was assigned to the A_{1g} mode, which is a clear indication of the magnetite form along with the bands observed at 174–193, 355, and 505 cm^{-1} for T_{2g} modes and 299–332 cm^{-1} for the E_g mode (where the 460–480 cm^{-1} band could be alternatively regarded as a T_{2g} band) (Figure 2A). On the other hand, the bands representing 355, 505, and 695 cm^{-1} could be regarded as the indication of T_1, E, and A_1 modes of maghemite. The strong peak observed at 719 cm^{-1} was attributed to the oxidation of Fe(II) to Fe(III) at the octahedral sites. Both the maghemite features and the oxidation at octahedral sites could be attributed to locally elevated temperatures induced by the micro-Raman technique, which is known to induce the change from magnetite to maghemite.[44]

Analysis in the 850–1750 cm^{-1} organic fingerprint region for dOA–IONPs could be performed only for 633 nm laser excitation because the 488 and 514 nm laser excitations did not provide the same band resolution in this region. On the other hand, Ac–IONPs exhibited a good band resolution under 488 and 514 nm excitations but suffered from a strong fluorescence background under 633 nm excitation. Therefore, the organic fingerprint region analysis of dOA–IONPs and Ac–IONPs is presented separately in Figure 2B,C. In Figure 2B, 633 nm-excited dOA–IONPs were compared to oleic acid, sodium oleate, iron oleate (IONP precursor), and iron(II) acetate to distinguish the differences between the complexation of oleate and acetate species with iron. The spectrum of dOA–IONPs was analyzed in five different regions and highlighted in different colors (deconvoluted view of the broad reference organic compound bands are provided for clear analysis in the Supporting Information Figure S3A–C). In Figure 2B, the orange band indicates the C=C bond of oleic acid,[50] which is observed as a minor shoulder in dOA–IONPs. The yellow band is particularly important because it represents the asymmetric carboxylate vibrations. This is due to the fact that

DOI: 10.1021/acs.langmuir.7b02743
Langmuir 2017, 33, 10351–10365

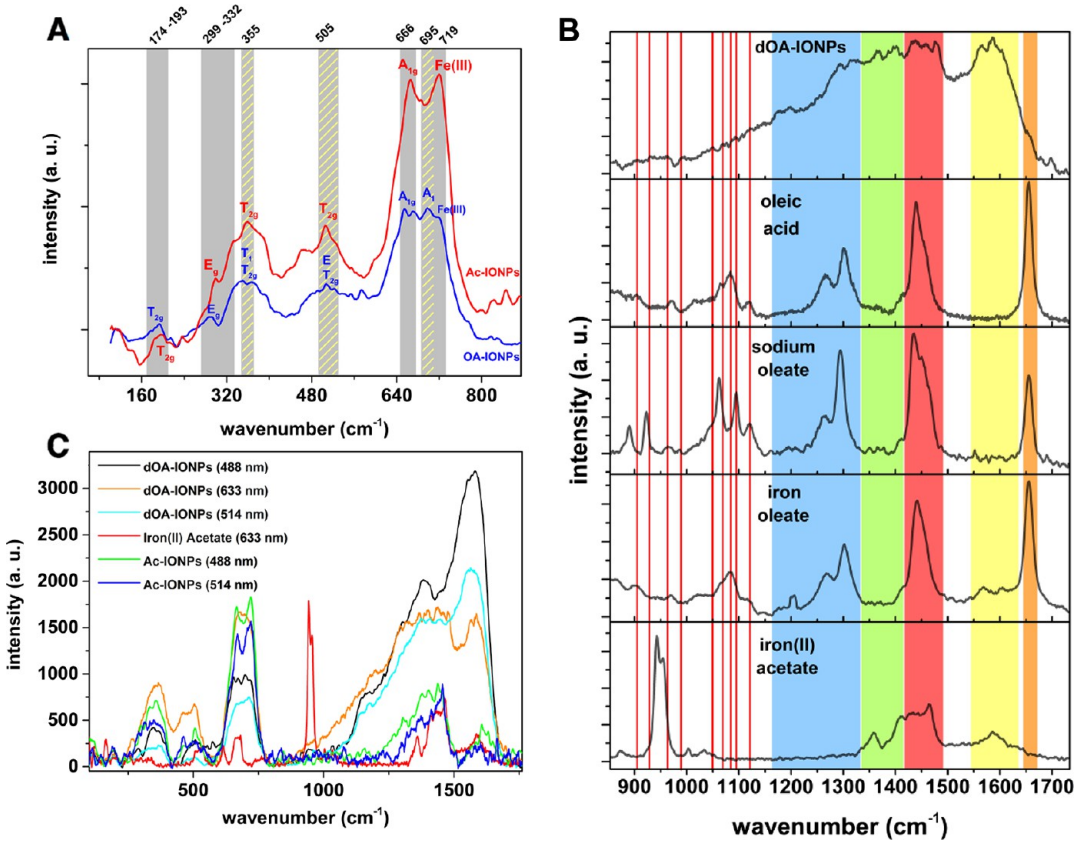

Figure 2. (A) Raman spectroscopy analysis of dOA–IONPs and Ac–IONPs at the iron oxide fingerprint region; (B) Raman spectroscopy analysis of dOA–IONPs in comparison to oleic acid, sodium oleate, iron oleate, and iron(II) acetate; and (C) comparison of the dOA–IONPs and Ac–IONPs under different laser excitations.

only iron oleate and iron acetate reveal these peaks, whereas oleic acid and sodium oleate lack them. The green region, where the dOA–IONPs have very intense peaks in comparison to all oleic acid/oleate references in the graph, was assigned to the symmetric stretching vibrations of carboxylates. This region also features very intense peaks for iron(II) acetate at 1412 and 1358 cm^{-1}, which have been assigned to both symmetric carboxylate stretching and CH_3 deformation modes for the iron(II) acetate complex.[51] On the other hand, for a cobalt acetate complex, a 1358 cm^{-1} peak was attributed to the symmetric carboxylate stretching.[52] Because of the different peak assignments made in previous studies and the distinct peak intensity exhibited by dOA–IONPs in this region, both 1401 and 1369 cm^{-1} peaks of dOA–IONPs were attributed to symmetric stretching vibrations of the carboxylates. The red band indicates the CH_3 stretching and bending vibrations. Peaks observed in this region for iron(II) acetate were found to be in agreement with the peaks previously reported for acetate complexes.[51,52] For the reference oleate/oleic acid compounds and dOA–IONPs, the red and blue regions are the indicators of the $-CH_2$ deformations, in agreement with the fatty acid metal complex vibrations.[50] Below the blue band region, strong C–C stretching and CH_2 rocking vibrations are observed. To make a clear visual comparison with all other samples, the peaks found for dOA–IONPS in this region are highlighted with red lines (Figure 2B). A list of all peaks analyzed at the 900–1700 cm^{-1} region in Figure 2C is provided in Figure S4A in the Supporting Information.

The band assignments made in Figure 2B were used as a guide for the second graph in Figure 2C, where the 488 and 514 nm-excited Ac–IONPs were compared to 488, 514, and 633 nm dOA–IONPs. This comparison clearly demonstrates the spectral intensity differences between the samples. In this comparison, we observed the following: (i) $\nu_{as}[COO^-]$ intensities (which corresponds to the yellow band region of Figure 2B) increase with the decreasing laser wavelengths for dOA–IONPs; (ii) increasing the wavelength from 488 to 514 nm results in a shift for the green and yellow band regions of the Ac–IONPs. The distance between the green and yellow band regions decreased without any notable difference in the peak intensities; and (iii) the identical spectral shapes of the Ac–IONPs and iron(II) acetate remarkably demonstrate the acetate–iron complex origin of Ac–IONPs (a list of peaks appearing at the 1300–1650 cm^{-1} region of the iron(II) acetate and Ac–IONPs sample for both 514 and 488 nm laser excitations is provided in Figure S4B,C in the Supporting Information). Vibrational modes in the iron oxide fingerprint region with minor shifts were found to be in agreement with all wavelengths used.

Briefly, FTIR and Raman analyses evidenced that the ethyl acetate saponification in the presence of IONPCs results in a ligand-exchange reaction between acetate ions and oleate on the surface of IONP building blocks of IONPCs, without altering the magnetite structure of IONPs.

Elemental Analysis of OA–IONPs and Ac–IONPs by TEM. To support the Raman and FTIR analyses that evidenced the acetate/oleate exchange, HRTEM and EELS measurements were carried out on OA–IONPs and Ac–IONPs. Fast Fourier transform (FFT) images of Ac–IONPs and OA–IONPs show that both samples contained only magnetite (Figure S5A–D in

DOI: 10.1021/acs.langmuir.7b02743
Langmuir 2017, 33, 10351–10365

the Supporting Information). Oxygen and iron content analyses by EELS confirmed that the composition of Ac−IONPs and OA−IONPs was identical (Figure S5E in the Supporting Information). This means that the ligand-exchange process mediated by ethyl acetate does not alter the structure of IONPs. On the other hand, the carbon content analysis by EELS demonstrated that the Ac−IONPs were coated with a uniform, amorphous-looking carbon shell in comparison to the OA−IONPs having brushlike, scattered carbon content (Figure 3A−D). Notably, despite the huge difference between the

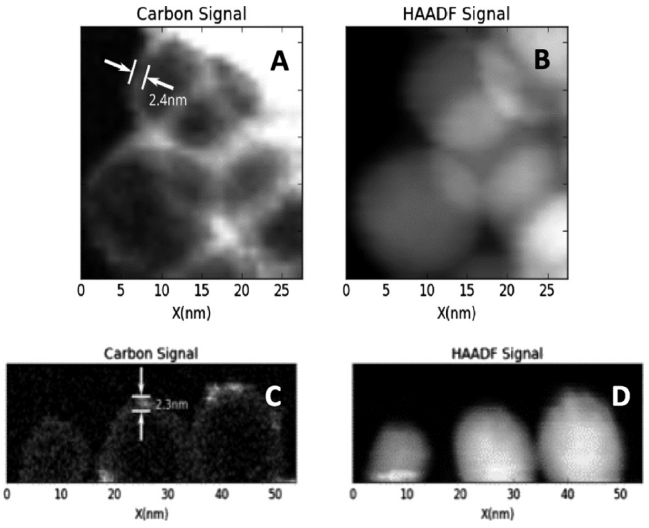

Figure 3. EELS analyses of carbon content: (A,B) acetate-coated IONPs and (C,D) oleic acid-coated IONPs.

acetate and oleic acid hydrocarbon contents (1:17), deposition of acetate in large amounts was evident from the similar carbon shell thicknesses in Ac−IONPs and OA−IONPs.

Characterization of IONPs@SiO_2 Structures. PREP1 process, as the extended version of the acetate/oleate ligand-exchange reaction by addition of silica precursors (TEOS and APTES), was analyzed by TEM. The results evidenced that high [CTAB]/[IONP] ratio conditions used in the PREP1 process yielded highly monodispersed IONPs@SiO_2 structures where the majority of the nanoparticles had single iron oxide cores, whereas few structures appeared to be having double or very rarely multiple cores (Figure 4A−C). The size distribution histogram was created by analyzing 1000 single-core structures. The normal size distribution model fitted to the histogram had a mean value of 58 and 4.2 nm full width at half-maximum, which confirmed the high-degree monodispersity achieved by the PREP1 process (Figure 4D).

IONPs@SiO_2 structures compared to Ac−IONPs and dOA−IONPs, in terms of the Raman spectrum in the iron oxide fingerprint region, showed only minor differences (Figure S3D in the Supporting Information). A_{1g} and Fe(III) bands are seen to match with those from Ac−IONPs and OA−IONPs (Figure 2A). However, $3T_{2g}$ and E_g bands observed at 190, 386, 492, and 303 cm^{-1} exhibited negligible shifts but significant intensity changes. Such results suggest that the silica coating had no chemical or physical influence on the IONP structure.

The chemical composition of the resulting core−shell structures obtained from the PREP1 reaction was further investigated by EELS measurements. Elemental analysis maps demonstrated that the core−shell structures were composed of

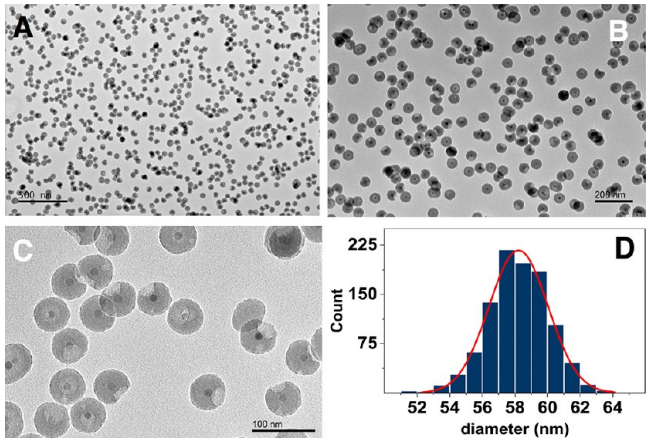

Figure 4. (A,B) Different level low-magnification TEM images of the IONPs@SiO_2 core−shell structures prepared by the PREP1 procedure, (C) high-magnification TEM image of IONPs@SiO_2 prepared by the PREP1 procedure, and (D) size distribution graph of IONPs@SiO_2 shown in image (A−C).

pure amorphous silicon oxide shells and iron oxide in the form of magnetite (Fe_3O_4) (Figure S6 in the Supporting Information). The Fe_3O_4 core composition is also supported by the HRTEM images of the core−shell structures and their corresponding FFTs (Figure S7 in the Supporting Information). Comparison of the two core−shell structures showed that there was no difference between their iron oxide compositions. Note that one of the core−shell structures was imaged through its apple bite-like cavity, showing no differences.

EELS fine structure parameters of the oxygen and iron edges were separately mapped (Figure S8 in the Supporting Information). A prepeak in the O K edge was observed for all samples, which is characteristic of magnetite. The prepeak intensity maps revealed homogenous composition of the IONPs. The same conclusion was obtained from the Fe $L_{2,3}$ white line parameter maps. Moreover, perfectly matching Fe $L_{2,3}$ edge spectral analysis of IONPs and IONPs@SiO_2 additionally proves that IONPs did not change their chemical composition after the coating process (Figure S8A in the Supporting Information).

TEM images of the PREP2 process revealed that low [CTAB]/[IONP] ratio conditions resulted in highly porous silica formations with uneven edges and a highly agglomerated state (Figure S9 in the Supporting Information). Iron oxide cores were not centered within the silica shells (Figure S9C in the Supporting Information). It was even possible to observe some silica shells that lost their iron oxide cores, thereby having empty cores (Figure S9C in the Supporting Information). PREP2 did not yield any core−shell structures with morphologies similar to those in PREP1, and silica shells were in a mesoporous form. The observed structures rarely consisted of single IONP cores but mostly of multiple (clustered) cores and many empty silica structures.

Comparison of PREP1 and PREP2 clearly demonstrated that the [CTAB]/[IONP] ratio was not the primary factor determining the formation of monodisperse IONPs@SiO_2. Existence of multicored structures in PREP2 clearly demonstrated that the IONP clustering problem persists despite using low [CTAB]/[IONP] ratio conditions in the PREP2 process. It was not possible to obtain CTAB-encapsulated OA−IONPs (CTA−OA−IONPs) individually,[14,19,28] which was previously

DOI: 10.1021/acs.langmuir.7b02743
Langmuir 2017, 33, 10351−10365

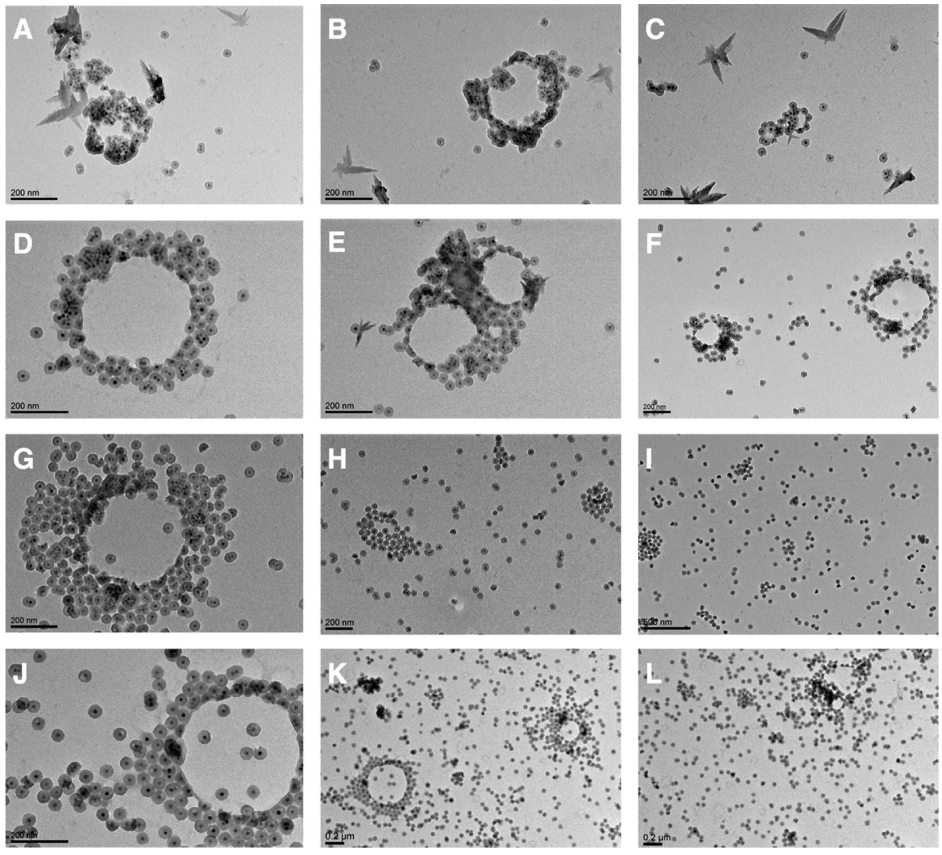

Figure 5. Time-resolved TEM observation of the silica-coating reaction progress: (A–C) 180 min after the silica precursor addition; (D–F) 195 min after the silica precursor addition; (G–I) 210 min after the silica precursor addition; and (J–L) 225 min after the silica precursor addition.

thought to be a prerequisite for the formation of monodispersed IONP@SiO_2.[19] In other words, PREP2 is a typical example of the OA–IONP clustering problem in the presence of CTA^+ molecules despite using a low [CTAB]/[IONP] ratio (Figure S9A in the Supporting Information). The PREP2 process proves that for a low concentration oil-in-water method, the exact determination of the [CTAB]/[IONP] ratio by costly and laborious techniques,[19] such as inductively coupled plasma–mass spectrometry analysis, is crucial. In contrast to PREP2, PREP1 proves to be an efficient, facile, and high-yielding method to obtain IONPs@SiO_2.

Because the above-demonstrated results evidenced that the IONP clustering problem was not the primary problem as previously thought, pH stabilization by ethyl acetate saponification was proved to play the primary role. Relatedly, "apple bite-like" cavities formed in almost every single-cored core–shell structure of PREP1 are a clear demonstration of the acetate buffering impact on silica formation (Figure 4C and Figure S10 in the Supporting Information). The existence of the "apple bite-like" cavities could be regarded as the "fingerprint" of the ethyl acetate buffering impact, which clearly distinguishes the high-concentration (PREP1) and low-concentration (PREP2) oil-in-water systems.

Time-Resolved TEM Investigation of the PREP1 Process. Although comparison between PREP1 and PREP2 processes evidenced that the ethyl acetate saponification reaction plays a key role in the appearance of the "apple bite-like" cavities, the mechanism behind the formation of these cavities requires further investigations. To reveal the additional factors that play a role in the formation of "apple bite-like" cavities, some samples were collected in intervals of 15 min, between 180 and 225 min after initiating the PREP1 process, and examined by TEM (Figure 5). Images showed formation of ringlike hollow structures 400–600 nm in diameter. The rings were formed by thin but heavily iron oxide-loaded silica shells at 180 min (Figure 5A,B). However, these iron oxide agglomerations were seen undergoing a deagglomeration process by spreading beside the rings that resulted in an increase in the ring widths till 210 min (Figure 5A–I). At 210 min, larger rings were seen to be still intact by keeping the core–shell structures attached (Figure 5G), however, smaller rings were already collapsed and started to release core–shell structures to the environment (Figure 5H). At 225 min, the number of particles around the rings started to decrease by the release of individual core–shell structures (Figure 5J,K). Core–shell structure release after 225 min gave rise to the highest amount of independent core–shell structures observed (Figure 5L). As the time progressed, the increase in the number of individual core–shell structures can be clearly observed (Figure 5C,F,I,L).

When the innermost core–shell nanoparticle layers of ringlike structures are closely observed, it is clearly seen that these core–shell particles are coated with hemispherical silica shells. Taking into account the highly hydrophilic nature of silica, we can conclude that the inner (hollow) region of the ringlike structures consists of a hydrophobic phase. On the other hand, the core–shell structures at the outer level of rings, which are far from the inner phase, have nearly full-spherical silica shells. However, the outermost particles are still connected with the adjacent particles via "necks" between the

DOI: 10.1021/acs.langmuir.7b02743
Langmuir 2017, 33, 10351–10365

respective silica shells. These observations suggest that the silica shell necking and the phase separation by the hydrophobic inner phase are the origin of the apple bite-like cavities observed on the silica shells.

It is noteworthy to mention that the ringlike structures shown in Figure 5 appear to be quite identical to the "on-grid" appearance of IONP-loaded polymersomes reported by Sanson et al.[53] The same appearance was reported for the polymersomes and magnetoliposomes having hydrophobic or hydrophilic lumens prepared with hydrophobic IONPs.[54,55] As reported by Sanson et al.,[53] ringlike structures can be observed as a consequence of the collapse of spherical magnetopolymersomes when the samples are dried on a TEM grid. To make sure whether we experienced a similar collapsing issue with the structures observed in Figure 5, we carried out an additional time-resolved TEM analysis. In comparison to flexible polymers used by Sanson et al.,[53] we had the advantage of using silica as the rigid material that can preserve the morphology of the nanoparticle clusters. By taking this advantage into account, we paid more attention to acidification of the PREP1 reaction environment that results in rapid reaction quenching and increases the silica sol rigidity. Acidification procedure was carefully performed during each subsequent centrifugal sample preparation process to make sure that maximum silica condensation and rigidity were achieved. Consequently, conventional TEM images of the acidified samples corresponding to 180−225 min of a typical PREP1 process revealed hemispherical IONPC formations (Figure 6A−D). This also explains that the ringlike structures, as it was

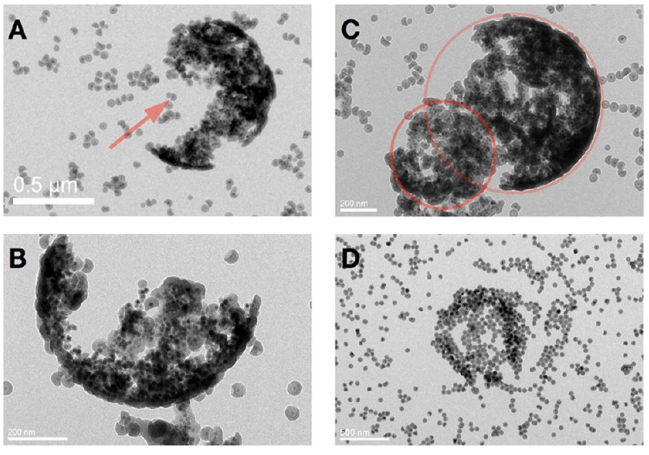

Figure 6. (A−C) Hemispheres of IONPCs partially coated with silica formed after 180 min of the PREP1 process. Red circles in image (C) indicate the positions of two hemispheres overlapping. (D) Hemisphere of IONPCs with almost full silica coating on every single IONP building block formed around 225 min of the PREP1 process. Hollow opening of the hemisphere positioned perpendicularly to the viewing angle. If "image A" was observed from the angle shown with the red arrow, the hemisphere would be positioned like the one in "image D".

for the case of Sanson et al.,[53] originated from the collapse of these hemispheres on the TEM grid. Collapse of the hemispheres took place, most likely because they were dried before the silica shells reached their full rigidity. Therefore, the large ringlike, hollow formations presented in Figure 5 must be regarded as a consequence of the collapsing hemispherical structures on TEM grids. Figure 6D clearly represents a preserved (noncollapsed) hemisphere structure in contrast to collapsed hemispheres in Figures 5G, J.

DLS and Cryo-TEM Investigations of the PREP1 Reaction. To make sure that the structures we observed in Figures 5 and 6 are also present in the bulk in identical sizes, we performed DLS experiments for the samples collected at 195 min of the PREP1 process. DLS analysis confirmed that mainly 400−600 nm sized objects were observable in both highly diluted and concentrated aqueous environments (Figure S11 in the Supporting Information). A wide size distribution was obtained from DLS measurements because the monodispersed core−shell structures start to be released from the clusters at 195 min of reaction, as we observed from the time-resolved TEM images (Figure 5D−F). On the other hand, IONPCs formed in various sizes contribute to the wide size distribution observed in DLS.

The origin of ringlike structures and hemispheres shown in Figures 5 and 6 were further investigated by cryo-TEM. These observations were carried out to detect and understand how they appear in an aqueous medium. Samples collected at 120 min of the PREP1 process gave an important clue that a fusion process took place between the IONPCs and independently coexisting vesicular structures (Figure 7). Notably, the existence

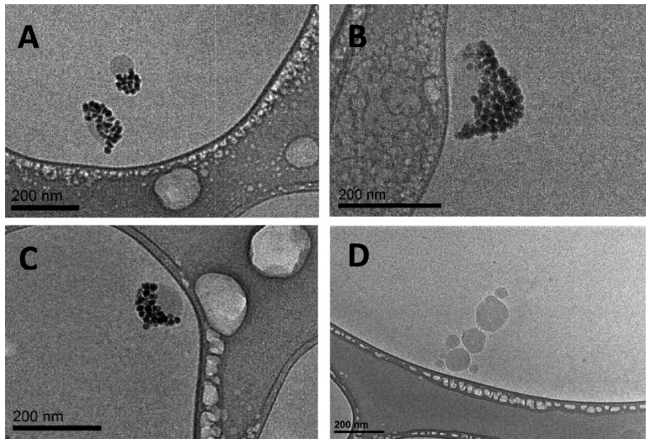

Figure 7. (A−C) Cryo-TEM images of the PREP1 process collected at 120 min of the reaction show the fusion of IONP clusters and silica nanoemulsions and (D) independently coexisting nanoemulsions found in the same sample before coalescence to IONPCs.

of the nanoemulsion droplets also explains the wide size distribution obtained by the DLS analysis. Fusion of vesicular structures (nanoemulsions) to the IONPCs was observed to change the spherical morphology of the clusters (Figure 7A,B). However, a completed fusion process was found to result in a nearly spherical hybrid nanoemulsion−IONPC formation (Figure 7C). Detection of these hybrid structures suggested that the ringlike structures (Figure 5) were formed after the drying process on the TEM grid.

The morphological transformations that IONPCs undergo after fusion with nanoemulsions indicate that the nanoemulsions were particularly attracted to the interior of the IONP clusters. In other words, the hydrophobic nanoemulsion phase had an affinity to the phase within the interior of IONPCs. Such an affinity relation highly resembles the coalescence of two "Janus colloidal capsules" that can be clearly observed on the microscale.[56] When two Janus colloidal capsules coalesce, colloids undergo a reorganization at the interface of an enlarged oil droplet and the surrounding liquid medium.[56] From Figure 7C, we observe a very similar behavior.

DOI: 10.1021/acs.langmuir.7b02743
Langmuir 2017, 33, 10351−10365

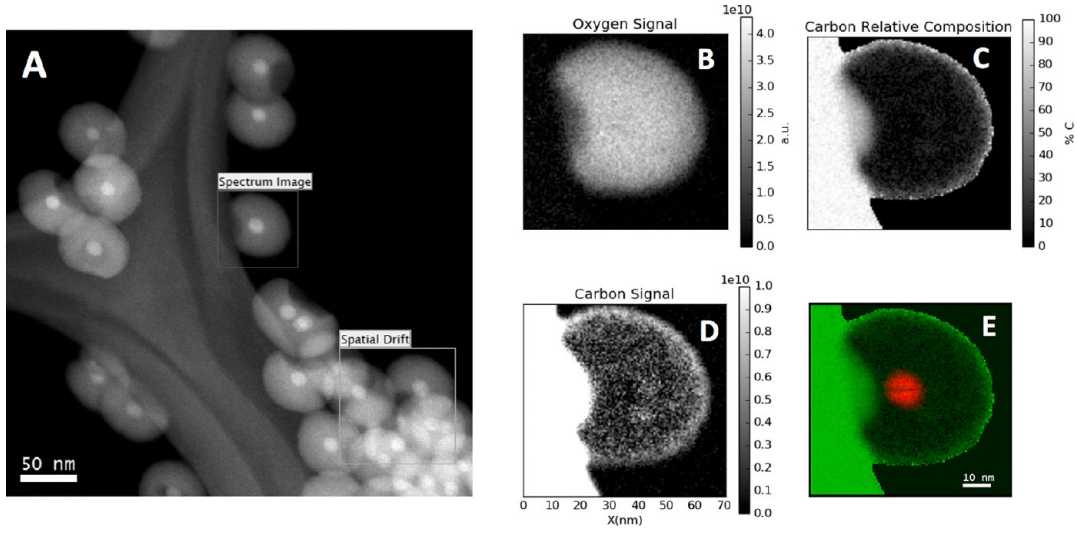

Figure 8. (A) HAADF image with a highlighted region where an EELS spectrum image was taken; (B) oxygen signal coming from silica; (C) carbon relative composition from the EELS SI; (D) carbon signal; and (E) colored map of carbon relative composition (green) with iron oxide core (red).

Nanoemulsion–IONPC hybrid morphology recovers to a nearly spherical shape when the fusion process is completed. Consequently, morphological transformations we herein observed are altogether strong indicators of IONPCs actually being oil-in-water "Janus colloidal capsules."[56] Nevertheless, the reason IONPCs appear to be hemispherical after fusion to the nanoemulsions could be attributed to the viscosity changes in the nanoemulsion phase because viscosity changes are known to play an important role in the coalescence dynamics of Janus colloidal capsules.[56] Changes in the nanoemulsion viscosity due to condensation of silica precursors most likely inhibit the IONPCs to undergo a full rearrangement around the nanoemulsions. Rapid condensation of silica precursors after fusion would be the most accurate scenario responsible from the viscosity increase. Although the "colloidal capsule" definition has been very recently suggested as the most universal term to describe Pickering-type emulsions,[57] IONPCs could be more specifically classified as "colloidosomes."[58] This is because the colloidosomes are described as stabilized Pickering emulsions.[59] When it is taken into account that IONPCs consist of OA–IONPs constrained at the oil–water interfaces by CTA^+ molecules, the "colloidosome" classification would be the most suitable term to describe IONPCs. Previously reported water-in-oil colloidosomes of iron oxide nanoparticles prepared in a similar manner in the presence of oil-soluble surfactants also strongly support the colloidosome nature of the IONPCs we herein report.[60]

Investigation of Silica Formation and Acetate/Oleate Ligand-Exchange Impact on IONPCs. Careful observations made on TEM images obtained from 180 min of the PREP1 process revealed that the silica-condensation reaction induced the formation of tiny iron oxide particles (Figure S12A,B in the Supporting Information). To confirm that such particles were indeed iron oxide and not any other contaminant or byproduct of the synthesis procedure, further EDX analyses were carried out on the 180 min sample. Because the TEM images were collected in a dark field, they allowed a clear differentiation of the higher atomic number iron cores from the lighter silica shells (Figure S13A,B in the Supporting Information). EDX spectra collected over the same area show that the only elements present on the sample are Fe, Si, and O (C and Cu being part of the grid), which clearly shows that the small particles had indeed iron oxide origin (Figure S13C–F in the Supporting Information). Additionally, cryo-TEM analysis of samples obtained from 120 min of the PREP1 process confirmed the existence of a thin shell covering each IONP building block of the IONPC hemisphere (Figure S12C,D in the Supporting Information). When the sample orientation was disturbed by melting the icy media with an intense electron beam, it was observed that these thin shells created tiny clusters (Figure S12E,F in the Supporting Information). The tiny clusters, formed as a consequence of the melting ice, were similar to tiny iron oxide particles observed in the 180 min sample (Figure S13A,B in the Supporting Information).

Existence of the tiny iron oxide nanoparticles at 120 min of the PREP1 process suggests that their formation was a consequence of the acetate/oleate ligand exchange because it was evidenced that silica condensation does not start at 120 min (Figure 7). Especially, the existence of a thin iron oxide shell observed in the cryo-TEM images suggests that the removal of oleate ligands from the IONPs cannot be simply described under the terms of a conventional "ligand exchange". Acetate/oleate exchange seems to proceed rather by removal of the outermost iron oxide surface from the IONPs by breakage. Such destructive effects of acetate ions on various iron oxide structures were previously reported.[61] If it is taken into account that the IONPCs were exposed to the acetate-rich reaction medium for 120 min (up to the start of the silica shell formations in PREP1) at elevated temperatures, acetate-induced damage of IONPs becomes a plausible scenario. However, EELS studies confirmed that the breakage by acetate ions in our study did not cause any observable chemical changes in IONPs (Figures S5 and S7 in the Supporting Information).

On the other hand, it was sensible to assume that these tiny iron oxide particles might have been present in the samples before the silica coating, although they were not observed in the TEM analyses in Figure 1A,B. To investigate whether the tiny iron oxide particles were the result of breakage by acetate ions or not, another batch of OA–IONPs with a very wide size distribution (ranging from 2 to 27 nm) was prepared (Figure S14 in the Supporting Information). The PREP1 reaction

DOI: 10.1021/acs.langmuir.7b02743
Langmuir 2017, 33, 10351–10365

performed in the presence of these IONPs with a wide size distribution demonstrated that both the smallest and largest iron oxide nanoparticles were coated with silica shells having the same thickness, regardless of their size. This indirect observation clearly suggests that there is an important difference between the tiny iron oxide particles formed as a result of acetate-induced IONP breakage and the formation of small IONPs as the thermal decomposition product. Because the tiny iron oxide particles observed as a result of acetate breakage did not have silica shells, we can conclude that the tiny iron oxide particles, observed in Figures S12 and S13, were formed as a consequence of the acetate-induced breakage.

Investigation of the Silica Formation Mechanism by Carbon Content Analyses. The existence and location of the carbon content have great importance to elucidate the long-considered role of CTA^+ as a structure-directing agent in siliceous material preparation. This information can demonstrate how surfactant molecules template the silica growth on the hydrophobic metal nanoparticle surfaces. As suggested by previously reported studies, aliphatic chains of the CTA^+ molecules interact with the aliphatic fatty acid chains covering the nanoparticle surface to form the oleate−CTA^+ bilayer.[14,15,19] Then, the cationic head groups of the CTA^+ molecules provide aqueous dispersibility. However, CTA^+ molecules later on interact with water-solubilized silicates to condense them into silica[14,15,19] in various morphologies.[16−18] In other words, the oleate−CTA^+ bilayer is physically capped by the silica shell as a consequence of the silica formation mechanism. On the other hand, our PREP1 process starts with the acetate/oleate exchange, and it was shown that the ligand exchange creates an acetate-based thick carbon shell in the absence of a silica shell. However, the fate of the initial acetate shell was unclear after the silica coating. When the previous hypotheses and our recent observations on acetate-induced ligand-exchange processes are taken into account together, some carbon content is expected between the silica shell and iron oxide core of the IONPs@SiO_2. To investigate the existence of this carbon content, either related to the oleate−CTA^+ bilayer or the acetate layer, we performed detailed EELS analyses on the individual core−shell structures prepared by the PREP1 process.

The first analysis shown in Figure 8 demonstrates that the outermost surface of silica shells is coated with carbon. The thick carbon shell seen at the particle edges was regarded as a clear indication of the CTA^+-templated silica growth mechanism (Figure 8C,E). The colored relative carbon composition map, including the IONP core, evidenced that the core was completely coated with silica (Figure 8E). Oxygen content from the silica shell confirmed its uniform structure (Figure 8B). A careful investigation of Figure 8D revealed a slight concentration of the carbon content around the core (an additional image of carbon concentrated around the core, obtained for a different particle, can be seen in Figure S8D in the Supporting Information). Further EELS analyses carried out on a particle after removal of surface CTA^+ molecules by dialysis confirmed that the outermost surface carbon content of IONPs@SiO_2 was removed to a great extent, and an inner carbon content indeed existed between the IONP core and the silica shell (Figure 9). Correspondingly, the XPS analysis performed for 0−840 min sputtering proved that the outermost carbon shell seen in Figure 8E belongs to the CTA^+ molecules (Figure S15 in the Supporting Information). With increasing sputtering time, existence of APTES molecules and acetate

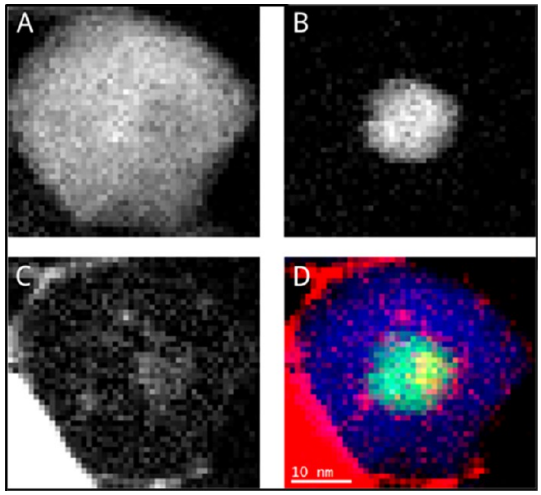

Figure 9. EELS analysis showing the (A) oxygen signal, (B) iron signal, (C) carbon signal, and (D) colored map of oxygen (blue), iron (green), and carbon (red).

species within the silica shell have been evidenced. Surprisingly, sodium found in the silica shell strongly suggests that the acetate species exists as a sodium salt within the silica shell.

When the chemical reactions taking place in a PREP1 process are discussed in detail, the acetate origin of the inner carbon shell can also be easily explained. Previously proposed hypotheses on the CTA^+-templated silica formation mechanisms required the silica precursors to be already hydrolyzed in the aqueous phase.[14,15,19,62,63] Such a hydrolysis prerequisite was considered essential for the interaction of negatively charged hydrolyzed silica precursors with positively charged CTA^+ molecules for silica condensation and growth. The initial hydrolysis of silica precursors can be achieved only by acid or base catalysis. However, acid/base catalyzed conditions do not correspond to our PREP1 reaction conditions because PREP1 was solely based on stabilizing pH of the reaction solution to neutral (pH ≈ 7) by the initial saponification reaction of ethyl acetate. In other words, the catalyst (NaOH) used in Kim and Ye et al. methods[14,19] for the hydrolysis of silica precursors was immediately consumed in the PREP1 process by rapid ethyl acetate saponification. Hydrolysis of the silica precursor (TEOS) after its addition to neutral aqueous solutions is known to proceed extremely slowly because of the immiscibility gap between water and hydrophobic TEOS.[64,65] Consequently, the introduction of the hydrophobic TEOS to the neutral aqueous solution of emulsifying CTA^+ molecules in the PREP1 process promotes nanoemulsion formation because of the oil-in-water behavior of the unhydrolyzed TEOS. Formation of these nanoemulsions was already evident in Figure 7D. Therefore, it can be concluded that the mechanism of silica formation in the PREP1 process is different from the previously laid down hypotheses[14,15,19] because unhydrolyzed silica precursors carried by the nanoemulsions are not capable of interacting with CTA^+. On the other hand, the above-presented results related to the acetate-induced breakage of the iron oxide particle surface and the thin iron oxide layer formation make the CTA^+−oleate bilayer removal from the nanoparticle surface a plausible scenario. Such a scenario makes it very unlikely that the inner carbon content seen in Figure 9D is related to the CTA^+−oleate bilayer. From the cryo-TEM analyses (Figure 7), we could conclude that the silica condensation did not start up to 120 min of the reaction. However, it was evident that the

DOI: 10.1021/acs.langmuir.7b02743
Langmuir 2017, 33, 10351−10365

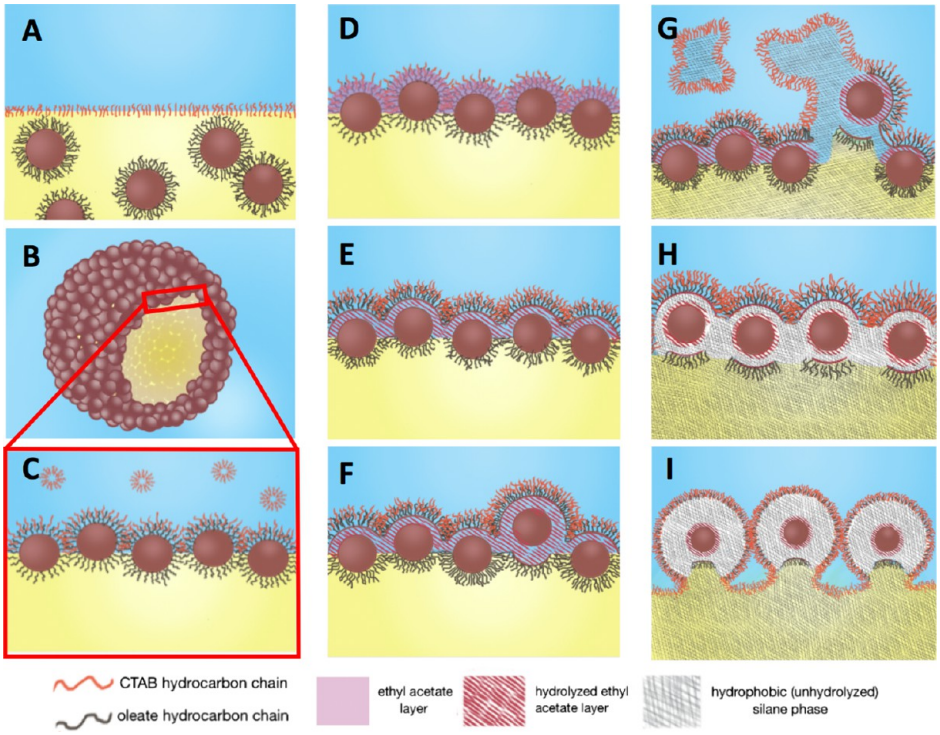

Figure 10. Micellar fusion mechanism leading to the formation of IONPs@acetate@SiO_2 structures: (A) initial mixtures of aqueous CTAB solution and OA–IONPs dispersion in chloroform showing the phase separation between the aqueous (blue) and hydrophobic (yellow) phase oil. CTAB molecules create a monolayer at the liquid–liquid interface; (B) after the evaporation of the organic phase, OA–IONPs are stabilized at the liquid–liquid interfaces, which results in the formation of IONPCs encapsulating the hydrophobic phase; (C) IONP building blocks of IONPCs at the liquid–liquid interface and some micellar structures of CTA^+ in the aqueous phase; (D) upon ethyl acetate addition into the solution, it is dispersed within the CTA^+–oleate bilayer on the surface of the clusters; (E) after ethyl acetate saponification, the resulting acetate ions interact with the iron oxide surface and break the iron oxide structure. The breakage results in thin iron oxide shell formations stabilized by the CTA^+–oleate bilayer; (F) later, the acetate layer penetrates the hydrophobic phase and removes the oleate-only coated surface of the IONPs. This results in fully dynamic IONP formations as seen for the fourth IONP from the left; (G) after addition of silica precursors, they form nanoemulsions with excess CTAB molecules/micelles in solution. They eventually attack the dynamic sites of the IONPCs (fourth IONP from the left), which they use as tiny gates to fuse with the hydrophobic core of the clusters. The fusion process takes place by the coalescence of CTA^+ monolayers of nanoemulsions to the CTA^+–oleate bilayers; (H) encapsulated silica precursors start to accumulate to space between the dynamic CTA^+–oleate bilayer and acetate-coated IONPs. Silica eventually starts to form, initially in the agglomerated form as observed in Figure 5A–C; (I) as time progresses, silica shell continues to grow, which will eventually lead to the formation of monodispersed IONPs@acetate@SiO_2.

silica condensation started at some point after the micellar fusion of the IONPCs and nanoemulsions. This means that the pH conditions (acidic or basic) essential for the hydrolysis of silica precursors must have been provided by the IONP clusters after fusion with nanoemulsions. Because the PREP1 process starts with the ethyl acetate saponification reaction, the pH conditions necessary to trigger the silica precursor hydrolysis were provided by the acetate layer that was already present before the fusion of nanoemulsions with IONPCs. Because the solvolysis of silica precursors by acetic acid is well-known,[66] acetic acid-induced silica formation stands out as the only possible scenario. Consequently, we can conclude that the inner carbon content observed in Figure 9D was formed by acetate ligands, and therefore, iron oxide–silica core–shell nanoparticles are hereinafter referred to as iron oxide–acetate–silica core–shell–shell nanoparticles (IONPs@acetate@SiO_2).

Proposed Mechanism for the Formation of Core–Shell Nanoparticles Mediated by IONPCs in Acetate Buffer. Exchange of oleate ligands by acetate ions on the IONP surfaces was a very fundamental observation to describe the mechanism behind the silica coating on the individual IONP surfaces. We demonstrated that the PREP1 reaction in the absence of silica precursors resulted in fully acetate-coated IONPs, and the acetate layer was preserved within the silica shell. On the other hand, by knowing that the IONPCs are in fact Pickering-type emulsions constrained at the oil–water interface (colloidosomes), we could elucidate that the acetate/oleate exchange leading to silica formation proceeded in five steps (Figure 10):

(i) A typical phase transfer of the OA–IONPs from the oil phase to aqueous phase by CTA^+ molecules (Figure 10A) results in the formation of IONPCs (Figure 10B) that we showed in Figure 1C,D. IONPCs are simply formed by the OA–IONPs that are partially encapsulated by CTA^+ molecules at the liquid–liquid interface (Figure 10C). When the ethyl acetate was introduced to the alkaline dispersion of IONPCs, the unhydrolyzed excess of the ethyl acetate phase directly interacted with the CTA^+–oleate bilayer on the IONP surfaces (Figure 10C,D). Formation of oil-in-water emulsion of ethyl acetate that was induced by the excess CTA^+ surfactant molecules would make such interactions highly possible.[32] However, a large fraction of ethyl acetate was immediately hydrolyzed in the aqueous phase because of the saponification reaction. It is highly feasible that ethyl acetate was exchanged continuously between the CTA^+–

DOI: 10.1021/acs.langmuir.7b02743
Langmuir 2017, 33, 10351–10365

oleate bilayer and the water phase, which results in the diffusion of acetate ions within the bilayer. As soon as the acetate ions gained access to the IONP surfaces, the acetate/oleate exchange must have proceeded via breakage of the iron oxide particles (Figure 10E);

(ii) We showed that the acetate/oleate exchange proceeded by breakage of iron oxide nanoparticles. Then, the broken iron oxide particles create a thin layer above the IONP surfaces (Supporting Information Figure S12C,D). Correspondingly, when the tiny iron oxide particles were formed by the acetate-induced breakage, the CTA^+–oleate bilayer must have been carried away along with the tiny iron oxide nanoparticles (Figure 10E). The attraction of iron-based thin shell to the IONP cluster surface could be assisted by the ionic and hydrogen bonds between the thin iron oxide shells and acetate ions on the IONP surfaces. Meanwhile, the hydrophobic portion of the IONPs that are still coated with oleate and oriented toward the hydrophobic phase within the IONPCs must have protected the IONPCs from undergoing a disassembly;

(iii) Eventually, the acetate-induced breakage must have taken place underneath the hydrophobic portion of the IONPs (Figure 10F). This must have removed the oleate-only coated portions of the IONPs that are oriented toward the hydrophobic core of the IONPCs. When the removal of oleate took place, individual iron oxide particles in clusters must have started to disassemble. Dynamic motions obtained by IONPCs after the disassembly must have facilitated the movement of their IONP building blocks toward the continuous aqueous phase. This also means that the CTA^+–oleate bilayer holding the thin iron oxide shells must have undergone dynamic rearrangements. Consequently, the displaced IONP building blocks of the IONPCs must have served as tiny gates between the nanoemulsions of silica precursors and the hydrophobic phase in the core of the IONPCs. It must be pointed out that the existence of "tiny gates" is the most accurate scenario because IONPCs were stable till 120 min of the PREP1 process when the nanoemulsion–IONPC hybrids start to form (Figure 7). In other words, IONPCs do not undergo a full disassembly process because of removal of the acetate/oleate bilayer from the surface;

(iv) Dynamic rearrangement of the CTA^+–oleate bilayer and formation of the tiny gates opening to the hydrophobic cores of IONPCs must have been the driving force for the fusion of nanoemulsions to the IONPCs. This appears to be an accurate scenario because similar fusion interactions of surfactant vesicles to the dynamic ligands on the nanoparticle surfaces are already known.[67] When the fusion process started (Figure 10G), the hydrophobic phase of silica precursors must have been transferred into the hydrophobic core of the IONPCs, and two hydrophobic phases must have merged inside the clusters (as in the case of coalescence of Janus colloidal capsules[56]). This could be the explanation why we observed that the emulsions seemed to be invading the IONP clusters in the cryo-TEM images (Figure 7A,B). Consequently, the rearrangement of IONPCs around the nanoemulsion phases must have resulted in the formation of IONPC–nanoemulsion hybrids that we observed in Figure 7C. Notably, additional CTA^+ molecules supplied to the IONPCs by nanoemulsions must have provided additional flexibility and dynamicity to the CTA^+–oleate bilayer for the dynamic rearrangement;

(v) Hydrolysis of the silica precursors must have started as soon as the IONPCs and nanoemulsion fusion was complete. What facilitated the formation of silica shells in spherical morphologies must have been the additional CTA^+ molecules supplied by the nanoemulsions to the CTA^+–oleate bilayers. This scenario is consistent with the observation of a thick carbon template around the silica shells in Figure 8C,E. These thick carbon shells in such high concentrations could be provided only by the CTA^+ surfactant molecules that are the largest source of carbon in the PREP1 process. Eventually, the hydrolysis of silica precursors on the IONP surfaces must have been catalyzed by the acetate ions.[66] The continuous accumulation of silica precursors from the hydrophobic core of the IONPCs to the space between the oleate–CTA^+ bilayer and IONP cores must have grown the silica shells (Figure 10H). Condensation of the precursor into silica around the IONP cores must have continued till the CTA^+–oleate bilayers lost their mobility (elasticity) and collapsed when the silica shells reached their maximum size (~60 nm). Release of individual IONPs@acetate@SiO_2 core–shell structures from the nanoemulsion–IONPC hybrids must have finally started, when the unity of CTA^+–oleate bilayers was lost (Figure 10I).

CONCLUSIONS

We have demonstrated that acetate ions formed in situ in the presence of IONPCs are efficient agents for ligand exchange with oleate-capping agents of the OA–IONPs. The acetate/oleate ligand exchange has been shown to be an efficient way for obtaining hydrophilic Ac–IONPs from hydrophobic OA–IONPs. More importantly, pH values stabilized by ethyl acetate/acetate buffer in high [CTAB]/[IONP] ratios have been shown to induce the formation of nanoemulsions of silica precursors, which are stable up to 2 h under refluxing conditions. This stability of the nanoemulsions has allowed us to observe the affinity of IONPCs to the hydrophobic phase (nanoemulsions) in an aqueous environment, which gives strong indications of IONPCs being oil-in-water Pickering-type emulsions, more specifically, "colloidosomes." The capability of IONPCs to encapsulate a hydrophobic medium in an aqueous environment and release it in the form of high-quality, monodispersed, hydrophilic core–shell nanostructures is expected to offer new venues for targeted drug-delivery of hydrophobic active agents.

Discovery of acetate ions within the core–shell nanoparticles has allowed us to elucidate that the formation of silica around the core–shell nanoparticles proceeds differently than the previously suggested inorganic surface-capping mechanisms in oil-in-water[14,19] or complete ligand exchange in water-in-oil systems.[21−24] More specifically, core–shell nanoparticles having apple bite-like cavities have been identified as iron oxide–acetate–silica core–shell–shell (IONPs@acetate@SiO_2) structures, which seem to be involving both covalent and physical interactions between iron oxide, acetate, and silicon oxide species. On the other hand, some features of the silica growth process have allowed us to conclude that the formation of

DOI: 10.1021/acs.langmuir.7b02743
Langmuir 2017, 33, 10351−10365

core−shell structures in the monodisperse form is primarily dictated by the presence of acetate ions and ethyl acetate/acetate-buffered pH stabilization rather than the [CTAB]/[IONP] ratio alone. Consequently, we herein propose a novel silica-condensation mechanism based on the existence of a dynamic CTA^+−oleate bilayer, which constitutes the most experimentally supported hypothesis on the formation of IONPs@SiO_2 in an oil-in-water system. In general, silica condensation is mediated by acetate ions, and the IONPCs are expected to serve as the most efficient and high-yielding method known to date for the preparation of high-quality IONPs@acetate@SiO_2.

■ ASSOCIATED CONTENT

Supporting Information

The Supporting Information is available free of charge on the ACS Publications website at DOI: 10.1021/acs.langmuir.7b02743.

FTIR data; phase separation; Raman spectra; resonant modes indexation (Raman); HRTEM, FFT, and Fe L edge; HRTEM and PCA; HRTEM−FFT; HRTEM−HAADF−EELS; TEM—PREP2; HRTEM—cavity formation; DLS measurements; time-resolved TEM—PREP1; EDX mapping and dark-field images PREP1; OA−IONPs with a wide size distribution; and XPS analysis (PDF)

■ AUTHOR INFORMATION

Corresponding Authors

*E-mail: kertmen@kth.se (A.K.).
*E-mail: toprak@kth.se (M.T.).

ORCID

Ahmet Kertmen: 0000-0002-6879-4404
Pau Torruella: 0000-0002-6864-4000
Emerson Coy: 0000-0002-4149-9720
Stefan Jurga: 0000-0002-1665-6077

Author Contributions

P.T. and E.C. equally contributed to this manuscript. Project conception: A.K., M.T., C.V., E.C., R.A., and S.M.; synthesis of nanoparticles: A.K.; TEM & HRTEM: P.T., S.E., F.P., E.C., and A.K.; cryo-TEM: G.N.; EELS: P.T., S.E., and F.P.; XPS: L.Y.; FTIR & Raman spectroscopies: A.K.; EDX: E.C.; DLS: J.G.; governing synthesis mechanism: A.K., M.T., and C.V.; manuscript preparation: A.K., P.T., E.C., M.T., J.G., R.A., S.M., and S.J.

Notes

The authors declare no competing financial interest.

■ ACKNOWLEDGMENTS

A.K. acknowledges the financial support provided by the PRELUDIUM programme of the National Science Centre of Poland (UMO-2015/17/N/NZ7/01087), European Union Human Capital Operational Programmes for the projects entitled "*The development of interdisciplinary doctoral studies at the Gdansk University of Technology in modern technologies*" (POKL.04.01.01-00-368/09), and "*The Centre for Advanced Studies—the development of interdisciplinary doctoral studies at the Gdansk University of Technology in the key areas of the Europe 2020 Strategy*" (POKL.04.03.00-00-238/12); P.T., S.E., and F.P. acknowledge the support of the Catalan Government (SGR2014-072) and the Ministry of Economy and Competitiveness of Spain (MAT2013-41506). Collaborations of Dr. Błażej Scheibe and Dr. Jacek Jenczyk from the NanoBioMedical Center in Adam Mickiewicz University and Dr. Zuzanna Pietralik from the Department of Macromolecular Physics in the Adam Mickiewicz University are also gratefully acknowledged.

■ REFERENCES

(1) Ling, D.; Hyeon, T. Chemical Design of Biocompatible Iron Oxide Nanoparticles for Medical Applications. *Small* **2013**, *9*, 1450−1466.
(2) Kim, T.; Hyeon, T. Applications of Inorganic Nanoparticles as Therapeutic Agents. *Nanotechnology* **2014**, *25*, 012001.
(3) Lee, N.; Yoo, D.; Ling, D.; Cho, M. H.; Hyeon, T.; Cheon, J. Iron Oxide Based Nanoparticles for Multimodal Imaging and Magnetoresponsive Therapy. *Chem. Rev.* **2015**, *115*, 10637−10689.
(4) Li, F.; Lu, J.; Kong, X.; Hyeon, T.; Ling, D. Dynamic Nanoparticle Assemblies for Biomedical Applications. *Adv. Mater.* **2017**, *29*, 1605897.
(5) Park, J.; An, K.; Hwang, Y.; Park, J.-G.; Noh, H.-J.; Kim, J.-Y.; Park, J.-H.; Hwang, N.-M.; Hyeon, T. Ultra-Large-Scale Syntheses of Monodisperse Nanocrystals. *Nat. Mater.* **2004**, *3*, 891−895.
(6) Bixner, O.; Lassenberger, A.; Baurecht, D.; Reimhult, E. Complete Exchange of the Hydrophobic Dispersant Shell on Monodisperse Superparamagnetic Iron Oxide Nanoparticles. *Langmuir* **2015**, *31*, 9198−9204.
(7) Lassenberger, A.; Bixner, O.; Gruenewald, T.; Lichtenegger, H.; Zirbs, R.; Reimhult, E. Evaluation of High-Yield Purification Methods on Monodisperse PEG-Grafted Iron Oxide Nanoparticles. *Langmuir* **2016**, *32*, 4259−4269.
(8) Zirbs, R.; Lassenberger, A.; Vonderhaid, I.; Kurzhals, S.; Reimhult, E. Melt-Grafting for the Synthesis of Core−shell Nanoparticles with Ultra-High Dispersant Density. *Nanoscale* **2015**, *7*, 11216−11225.
(9) Kurzhals, S.; Zirbs, R.; Reimhult, E. Synthesis and Magneto-Thermal Actuation of Iron Oxide Core−PNIPAM Shell Nanoparticles. *ACS Appl. Mater. Interfaces* **2015**, *7*, 19342−19352.
(10) Lee, J. E.; Lee, N.; Kim, T.; Kim, J.; Hyeon, T. Multifunctional Mesoporous Silica Nanocomposite Nanoparticles for Theranostic Applications. *Acc. Chem. Res.* **2011**, *44*, 893−902.
(11) Lee, N.; Cho, H. R.; Oh, M. H.; Lee, S. H.; Kim, K.; Kim, B. H.; Shin, K.; Ahn, T.-Y.; Choi, J. W.; Kim, Y.-W.; Choi, S. H.; Hyeon, T. Multifunctional Fe_3O_4/TaO_X Core/Shell Nanoparticles for Simultaneous Magnetic Resonance Imaging and X-Ray Computed Tomography. *J. Am. Chem. Soc.* **2012**, *134*, 10309−10312.
(12) Amstad, E.; Textor, M.; Reimhult, E. Stabilization and Functionalization of Iron Oxide Nanoparticles for Biomedical Applications. *Nanoscale* **2011**, *3*, 2819−2843.
(13) Amstad, E.; Reimhult, E. Nanoparticle Actuated Hollow Drug Delivery Vehicles. *Nanomedicine* **2012**, *7*, 145−164.
(14) Kim, J.; Kim, H. S.; Lee, N.; Kim, T.; Kim, H.; Yu, T.; Song, I. C.; Moon, W. K.; Hyeon, T. Multifunctional Uniform Nanoparticles Composed of a Magnetite Nanocrystal Core and a Mesoporous Silica Shell for Magnetic Resonance and Fluorescence Imaging and for Drug Delivery. *Angew. Chem., Int. Ed.* **2008**, *47*, 8438−8441.
(15) Fan, H. Self-Assembly of Ordered, Robust, Three-Dimensional Gold Nanocrystal/Silica Arrays. *Science* **2004**, *304*, 567−571.
(16) Beck, J. S.; Vartuli, J. C.; Roth, W. J.; Leonowicz, M. E.; Kresge, C. T.; Schmitt, K. D.; Chu, C. T. W.; Olson, D. H.; Sheppard, E. W.; McCullen, S. B.; Higgins, J. B.; Schlenker, J. L. A New Family of Mesoporous Molecular Sieves Prepared with Liquid Crystal Templates. *J. Am. Chem. Soc.* **1992**, *114*, 10834−10843.
(17) Yanagisawa, T.; Shimizu, T.; Kuroda, K.; Kato, C. The Preparation of Alkyltriinethylaininonium−Kaneinite Complexes and Their Conversion to Microporous Materials. *Bull. Chem. Soc. Jpn.* **1990**, *63*, 988−992.

DOI: 10.1021/acs.langmuir.7b02743
Langmuir 2017, 33, 10351−10365

(18) Kresge, C. T.; Leonowicz, M. E.; Roth, W. J.; Vartuli, J. C.; Beck, J. S. Ordered Mesoporous Molecular Sieves Synthesized by a Liquid-Crystal Template Mechanism. *Nature* **1992**, *359*, 710−712.
(19) Ye, F.; Laurent, S.; Fornara, A.; Astolfi, L.; Qin, J.; Roch, A.; Martini, A.; Toprak, M. S.; Muller, R. N.; Muhammed, M. Uniform Mesoporous Silica Coated Iron Oxide Nanoparticles as a Highly Efficient, Nontoxic MRI T2 Contrast Agent with Tunable Proton Relaxivities. *Contrast Media Mol. Imaging* **2012**, *7*, 460−468.
(20) Saha, K.; Kim, S. T.; Yan, B.; Miranda, O. R.; Alfonso, F. S.; Shlosman, D.; Rotello, V. M. Surface Functionality of Nanoparticles Determines Cellular Uptake Mechanisms in Mammalian Cells. *Small* **2013**, *9*, 300−305.
(21) Ding, H. L.; Zhang, Y. X.; Wang, S.; Xu, J. M.; Xu, S. C.; Li, G. H. Fe_3O_4@SiO_2 Core/Shell Nanoparticles: The Silica Coating Regulations with a Single Core for Different Core Sizes and Shell Thicknesses. *Chem. Mater.* **2012**, *24*, 4572−4580.
(22) Vogt, C.; Toprak, M. S.; Muhammed, M.; Laurent, S.; Bridot, J.-L.; Müller, R. N. High Quality and Tuneable Silica Shell−magnetic Core Nanoparticles. *J. Nanopart. Res.* **2010**, *12*, 1137−1147.
(23) Koole, R.; van Schooneveld, M. M.; Hilhorst, J.; de Mello Donegá, C.; 'T Hart, D. C.; van Blaaderen, A.; Vanmaekelbergh, D.; Meijerink, A. On the Incorporation Mechanism of Hydrophobic Quantum Dots in Silica Spheres by a Reverse Microemulsion Method. *Chem. Mater.* **2008**, *20*, 2503−2512.
(24) Darbandi, M.; Thomann, R.; Nann, T. Single Quantum Dots in Silica Spheres by Microemulsion Synthesis. *Chem. Mater.* **2005**, *17*, 5720−5725.
(25) Chen, Y.; Bose, A.; Bothun, G. D. Controlled Release from Bilayer-Decorated Magnetoliposomes via Electromagnetic Heating. *ACS Nano* **2010**, *4*, 3215−3221.
(26) De Cuyper, M.; Joniau, M. Magnetoliposomes. Formation and Structural Characterization. *Eur. Biophys. J.* **1988**, *15*, 311−319.
(27) Amstad, E.; Kohlbrecher, J.; Müller, E.; Schweizer, T.; Textor, M.; Reimhult, E. Triggered Release from Liposomes through Magnetic Actuation of Iron Oxide Nanoparticle Containing Membranes. *Nano Lett.* **2011**, *11*, 1664−1670.
(28) Qiu, P.; Jensen, C.; Charity, N.; Towner, R.; Mao, C. Oil Phase Evaporation-Induced Self-Assembly of Hydrophobic Nanoparticles into Spherical Clusters with Controlled Surface Chemistry in an Oil-in-Water Dispersion and Comparison of Behaviors of Individual and Clustered Iron Oxide Nanoparticles. *J. Am. Chem. Soc.* **2010**, *132*, 17724−17732.
(29) Lu, Z.; Yin, Y. Colloidal Nanoparticle Clusters: Functional Materials by Design. *Chem. Soc. Rev.* **2012**, *41*, 6874.
(30) Bixner, O.; Reimhult, E. Controlled Magnetosomes: Embedding of Magnetic Nanoparticles into Membranes of Monodisperse Lipid Vesicles. *J. Colloid Interface Sci.* **2016**, *466*, 62−71.
(31) Tadyszak, K.; Kertmen, A.; Coy, E.; Andruszkiewicz, R.; Milewski, S.; Kardava, I.; Scheibe, B.; Jurga, S.; Chybczyńska, K. Spectroscopic and Magnetic Studies of Highly Dispersible Superparamagnetic Silica Coated Magnetite Nanoparticles. *J. Magn. Magn. Mater.* **2017**, *433*, 254−261.
(32) Yang, W.; Li, B. A Novel Liquid Template Corrosion Approach for Layered Silica with Various Morphologies and Different Nanolayer Thicknesses. *Nanoscale* **2014**, *6*, 2292−2298.
(33) Huh, Y.-M.; Jun, Y.-w.; Song, H.-T.; Kim, S.; Choi, J.-s.; Lee, J.-H.; Yoon, S.; Kim, K.-S.; Shin, J.-S.; Suh, J.-S.; Cheon, J. In Vivo Magnetic Resonance Detection of Cancer by Using Multifunctional Magnetic Nanocrystals. *J. Am. Chem. Soc.* **2005**, *127*, 12387−12391.
(34) Chen, Z. P.; Zhang, Y.; Zhang, S.; Xia, J. G.; Liu, J. W.; Xu, K.; Gu, N. Preparation and Characterization of Water-Soluble Monodisperse Magnetic Iron Oxide Nanoparticles via Surface Double-Exchange with DMSA. *Colloids Surf., A* **2008**, *316*, 210−216.
(35) Davis, K.; Qi, B.; Witmer, M.; Kitchens, C. L.; Powell, B. A.; Mefford, O. T. Quantitative Measurement of Ligand Exchange on Iron Oxides via Radiolabeled Oleic Acid. *Langmuir* **2014**, *30*, 10918−10925.
(36) Davis, K.; Cole, B.; Ghelardini, M.; Powell, B. A.; Mefford, O. T. Quantitative Measurement of Ligand Exchange with Small-Molecule Ligands on Iron Oxide Nanoparticles via Radioanalytical Techniques. *Langmuir* **2016**, *32*, 13716−13727.
(37) Smolensky, E. D.; Park, H.-Y. E.; Berquó, T. S.; Pierre, V. C. Surface Functionalization of Magnetic Iron Oxide Nanoparticles for MRI Applications—Effect of Anchoring Group and Ligand Exchange Protocol. *Contrast Media Mol. Imaging* **2010**, *6*, 189−199.
(38) Pichon, B. P.; Demortière, A.; Pauly, M.; Mougin, K.; Derory, A.; Bégin-Colin, S. 2D Assembling of Magnetic Iron Oxide Nanoparticles Promoted by SAMs Used as Well-Addressed Surfaces. *J. Phys. Chem. C* **2010**, *114*, 9041−9048.
(39) Egerton, R. F. *Electron Energy-Loss Spectroscopy in the Electron Microscope*; Springer US: Boston, MA, 2011.
(40) Provencher, S. W. CONTIN: A General Purpose Constrained Regularization Program for Inverting Noisy Linear Algebraic and Integral Equations. *Comput. Phys. Commun.* **1982**, *27*, 229−242.
(41) Urata, C.; Aoyama, Y.; Tonegawa, A.; Yamauchi, Y.; Kuroda, K. Dialysis Process for the Removal of Surfactants to Form Colloidal Mesoporous Silica Nanoparticles. *Chem. Commun.* **2009**, 5094−5096.
(42) Schindelin, J.; Arganda-Carreras, I.; Frise, E.; Kaynig, V.; Longair, M.; Pietzsch, T.; Preibisch, S.; Rueden, C.; Saalfeld, S.; Schmid, B.; Tinevez, J.-Y.; White, D. J.; Hartenstein, V.; Eliceiri, K.; Tomancak, P.; Cardona, A. Fiji: An Open-Source Platform for Biological-Image Analysis. *Nat. Methods* **2012**, *9*, 676−682.
(43) Shebanova, O. N.; Lazor, P. Raman Spectroscopic Study of Magnetite (FeFe2O4): A New Assignment for the Vibrational Spectrum. *J. Solid State Chem.* **2003**, *174*, 424−430.
(44) Chamritski, I.; Burns, G. Infrared- and Raman-Active Phonons of Magnetite, Maghemite, and Hematite: A Computer Simulation and Spectroscopic Study. *J. Phys. Chem. B* **2005**, *109*, 4965−4968.
(45) Jacintho, G. V. M.; Brolo, A. G.; Corio, P.; Suarez, P. A. Z.; Rubim, J. C. Structural Investigation of MFe_2O_4 (M = Fe, Co) Magnetic Fluids. *J. Phys. Chem. C* **2009**, *113*, 7684−7691.
(46) White, W. B.; DeAngelis, B. A. Interpretation of the Vibrational Spectra of Spinels. *Spectrochim. Acta, Part A* **1967**, *23*, 985−995.
(47) Gasparov, L. V.; Tanner, D. B.; Romero, D. B.; Berger, H.; Margaritondo, G.; Forró, L. Infrared and Raman Studies of the Verwey Transition in Magnetite. *Phys. Rev. B: Condens. Matter Mater. Phys.* **2000**, *62*, 7939−7944.
(48) de Faria, D. L. A.; Venâncio Silva, S.; de Oliveira, M. T. Raman Microspectroscopy of Some Iron Oxides and Oxyhydroxides. *J. Raman Spectrosc.* **1997**, *28*, 873−878.
(49) da Silva, S. W.; Melo, T. F. O.; Soler, M. A. G.; Lima, E. C. D.; da Silva, M. F.; Morais, P. C. Stability of Citrate-Coated Magnetite and Cobalt-Ferrite Nanoparticles Under Laser Irradiation: A Raman Spectroscopy Investigation. *IEEE Trans. Magn.* **2003**, *39*, 2645−2647.
(50) Otero, V.; Sanches, D.; Montagner, C.; Vilarigues, M.; Carlyle, L.; Lopes, J. A.; Melo, M. J. Characterisation of Metal Carboxylates by Raman and Infrared Spectroscopy in Works of Art. *J. Raman Spectrosc.* **2014**, *45*, 1197−1206.
(51) Edwards, H. G. M.; Lewis, I. R. Vibrational Spectroscopic Studies of iron(II) Acetate. *J. Mol. Struct.* **1993**, *296*, 15−20.
(52) Nickolov, Z.; Georgiev, G.; Stoilova, D.; Ivanov, I. Raman and IR Study of Cobalt Acetate Dihydrate. *J. Mol. Struct.* **1995**, *354*, 119−125.
(53) Sanson, C.; Diou, O.; Thévenot, J.; Ibarboure, E.; Soum, A.; Brûlet, A.; Miraux, S.; Thiaudière, E.; Tan, S.; Brisson, A.; Dupuis, V.; Sandre, O.; Lecommandoux, S. Doxorubicin Loaded Magnetic Polymersomes: Theranostic Nanocarriers for MR Imaging and Magneto-Chemotherapy. *ACS Nano* **2011**, *5*, 1122−1140.
(54) Beaune, G.; Levy, M.; Neveu, S.; Gazeau, F.; Wilhelm, C.; Ménager, C. Different Localizations of Hydrophobic Magnetic Nanoparticles within Vesicles Trigger Their Efficiency as Magnetic Nano-Heaters. *Soft Matter* **2011**, *7*, 6248.
(55) Arosio, P.; Thévenot, J.; Orlando, T.; Orsini, F.; Corti, M.; Mariani, M.; Bordonali, L.; Innocenti, C.; Sangregorio, C.; Oliveira, H.; Lecommandoux, S.; Lascialfari, A.; Sandre, O. Hybrid Iron Oxide-Copolymer Micelles and Vesicles as Contrast Agents for MRI: Impact of the Nanostructure on the Relaxometric Properties. *J. Mater. Chem. B* **2013**, *1*, 5317.

DOI: 10.1021/acs.langmuir.7b02743
Langmuir 2017, 33, 10351−10365

(56) Rozynek, Z.; Mikkelsen, A.; Dommersnes, P.; Fossum, J. O. Electroformation of Janus and Patchy Capsules. *Nat. Commun.* **2014**, *5*, 3945.
(57) Bollhorst, T.; Rezwan, K.; Maas, M. Colloidal Capsules: Nano- and Microcapsules with Colloidal Particle Shells. *Chem. Soc. Rev.* **2017**, *46*, 2091−2126.
(58) Dinsmore, A. D.; Hsu, M. F.; Nikolaides, M. G.; Marquez, M.; Bausch, A. R.; Weitz, D. A. Colloidosomes: Selectively Permeable Capsules Composed of Colloidal Particles. *Science* **2002**, *298*, 1006−1009.
(59) Morse, A. J.; Giakoumatos, E. C.; Tan, S.-Y.; Webber, G. B.; Armes, S. P.; Ata, S.; Wanless, E. J. Giant pH-Responsive Microgel Colloidosomes: Preparation, Interaction Dynamics and Stability. *Soft Matter* **2016**, *12*, 1477−1486.
(60) Bollhorst, T.; Shahabi, S.; Wörz, K.; Petters, C.; Dringen, R.; Maas, M.; Rezwan, K. Bifunctional Submicron Colloidosomes Coassembled from Fluorescent and Superparamagnetic Nanoparticles. *Angew. Chem., Int. Ed.* **2015**, *54*, 118−123.
(61) Rose, J.; Cortalezzi-Fidalgo, M. M.; Moustier, S.; Magnetto, C.; Jones, C. D.; Barron, A. R.; Wiesner, M. R.; Bottero, J.-Y. Synthesis and Characterization of Carboxylate−FeOOH Nanoparticles (Ferroxanes) and Ferroxane-Derived Ceramics. *Chem. Mater.* **2002**, *14*, 621−628.
(62) Brinker, C. J. Hydrolysis and Condensation I: Nonsilicates. *Sol-Gel Science. The Physics and Chemistry of Sol−Gel Processing*; Academic Press, 1990; Chapter 2, pp 21−96.
(63) Schubert, U. Chemistry and Fundamentals of the Sol-Gel Process. *The Sol-Gel Handbook*; John Wiley & Sons, 2015; Vols. *1*−*3*, pp 1−28.
(64) Donatti, D. A.; Vollet, D. R. Study of the Hydrolysis of TEOS-TMOS Mixtures under Ultrasound Stimulation. *J. Non-Cryst. Solids* **1996**, *204*, 301−304.
(65) Vollet, D. R.; Donatti, D. A.; Campanha, J. R. A Kinetic Model for the Ultrasound Catalyzed Hydrolysis of Solventless TEOS-Water Mixtures and the Role of the Initial Additions of Ethanol. *J. Sol-Gel Sci. Technol.* **1996**, *6*, 57−63.
(66) Orel, B.; Ješe, R.; Štangar, U. L.; Grdadolnik, J.; Puchberger, M. Infrared Attenuated Total Reflection Spectroscopy Studies of Aprotic Condensation of (EtO)3SiRSi(OEt)3 and RSi(OEt)3 Systems with Carboxylic Acids. *J. Non-Cryst. Solids* **2005**, *351*, 530−549.
(67) Lee, H.-Y.; Shin, S. H. R.; Abezgauz, L.; Lewis, S. A.; Chirsan, A. M.; Danino, D.; Bishop, K. J. M. Correction to "Integration of Gold Nanoparticles into Bilayer Structures via Adaptive Surface Chemistry". *J. Am. Chem. Soc.* **2013**, *135*, 12476.

DOI: 10.1021/acs.langmuir.7b02743
Langmuir 2017, 33, 10351−10365